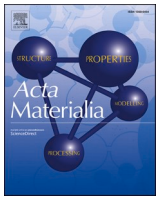
Acta Materialia 270 (2024) 119829



Contents lists available at ScienceDirect

Acta Materialia

journal homepage: www.elsevier.com/locate/actamat



Full length article

Morphology, mechanical properties, and oxidation behavior of stoichiometric $Ti_{0.33-x}Al_xB_{0.67}$ coatings (x = 0.04, 0.15, 0.21, and 0.28)

Amir Hossein Navidi Kashani [a,*], Marcus Hans [a], Sebastian Lellig [a,c], Damian M. Holzapfel [a], Lukas Löfler [a], Stanislav Mráz [a], Daniel Primetzhofer [b], Johann Michler [c], Jochen M. Schneider [a]

[a] Materials Chemistry, RWTH Aachen University, Kopernikusstr. 10, D-52074 Aachen, Germany
[b] Department of Physics and Astronomy, Uppsala University, Lägerhyddsvägen 1, S-75120 Uppsala, Sweden
[c] Empa, Materials Science and Technology, Laboratory for Mechanics of Materials and Nanostructures, Feuerwerkerstrasse 39, 3602 Thun, Switzerland

ARTICLE INFO

Keywords:
Stoichiometric $Ti_{0.33-x}Al_xB_{0.67}$ coatings
High temperature oxidation
TiAlN
Hard coatings

ABSTRACT

Stoichiometric $Ti_{0.33-x}Al_xB_{0.67}$ coatings with x = 0.04, 0.15, 0.21, and 0.28 were synthesized by magnetron sputtering and characterized regarding phase formation, mechanical properties, and oxidation behavior. By increasing the Al concentration from 4 to 28 at.%, the measured elastic modulus (496 ± 19 GPa) and unit cell volume (25.646 Å^3) decreased by 33 and 0.8 %, respectively. The Al concentration induced changes in measured elastic modulus and unit cell volume are in very good agreement with *ab initio* predictions, as the maximum deviations between experiment and theory, observed here, are 12 and 1.1 %, respectively. The corresponding hardness values decreased by 45 % from 22 ± 1 to 12 ± 1 GPa.

The oxidation experiments were performed in ambient air at 700, 800, and 900 °C for 1, 4, and 8 h. Analysis by scanning transmission electron microscopy (STEM) revealed a bimodal, strongly Al concentration-dependent oxidation behavior where films containing ≤ 15 at.% of Al form a porous, non-passivating crystalline oxide scale containing Ti-rich as well as Al-rich oxide regions, while the formation of a passivating, dense, X-ray amorphous oxide scale was observed for films containing ≥ 21 at.% of Al. Coincident with the passive scale formation for Al concentrations ≥ 21 at.%, the elastic modulus decreases by ≥ 32.6 % compared to TiB_2 and can be rationalized based on Al concentration induced bond weakening as revealed by the concomitant cohesive energy reduction of ≥ 22 %.

1. Introduction

Bulk titanium diboride (TiB_2) exhibits - from an application perspective – a promising property combination: High thermal stability [1,2] with a melting point of 3225 ± 20 °C [3,4] and hardness values in the range of 21 [5] to 29 [6] GPa, while the elastic moduli range between 530 [7] to 565 GPa [4] and are hence between c-BN and α-Al_2O_3 with 660 and 400 GPa, respectively [8]. The bulk thermal conductivity is 96 W/m•K [4] larger than for Ni (65–90 W/m•K) [9] and the relatively low bulk electrical resistivity of 9–15 μmΩ [10] is on par with 13.5 μmΩ of Ta [11]. TiB_2 crystallizes in an AlB_2-type structure, where boron atoms are fashioned in a hexagonal structure interleaved by Ti layers leading to the formation of strong covalent bonding (Ti-B and B-B) with metallic contributions (Ti-Ti) [4]. While the strong covalent-ionic interactions explain the thermal stability and mechanical behavior of TiB_2 [12], the metallic bond character promotes electrical and thermal conductivity [13,14].

Due to the above discussed combination of properties, TiB_2 coatings are applied as coatings for wear and corrosion protection [15–18] and as diffusion barriers in microelectronics [19–22]. The most commonly used physical vapor deposition (PVD) technique to fabricate TiB_2 coatings is direct current magnetron sputtering (DCMS) [2,23–25]; however; other magnetron sputtering methods such as radio frequency magnetron sputtering (RFMS) [26,27] and high-power impulse magnetron sputtering (HiPIMS) have [28–32] also been utilized. From the published literature, it is evident that the deposition of stoichiometric coatings through controlling the B/M ratio during film synthesis by magnetron sputtering using compound or composite targets is challenging: For example, TiB_x films deposited by DCMS from a compound target are often reported to be B-rich (B/M > 2) [2,23,33–35]. Neidhardt *et al.* [35] showed that this deficiency of Ti may be explained by the preferential emission of sputtered B along the target normal. Furthermore, it was

* Corresponding author.
E-mail address: navidi@mch.rwth-aachen.de (A.H. Navidi Kashani).

https://doi.org/10.1016/j.actamat.2024.119829
Received 11 January 2024; Received in revised form 9 March 2024; Accepted 10 March 2024
Available online 16 March 2024
1359-6454/© 2024 The Author(s). Published by Elsevier Ltd on behalf of Acta Materialia Inc. This is an open access article under the CC BY-NC-ND license (http://creativecommons.org/licenses/by-nc-nd/4.0/).

demonstrated that the angular distribution functions of sputtered Ti and B atoms, affecting the ratio between Ti and B measured in the as-deposited films, is also modified by gas-phase scattering during transport from the target to the substrate. Mayrhofer *et al.* [2] reported that DCMS deposition using a TiB_2 target resulted in TiB_x coatings with $x = 2.4 – 3.2$ exhibiting columnar morphologies (average feature size of approximately 20 nm) which consist of approximately 5 nm-sized sub-columns of stoichiometric TiB_2 surrounded by a B-rich tissue phase. Contrarily, B-deficient TiB_x coatings grown by HiPIMS from a TiB_2 target were reported by Thörnberg *et al.* [32] and exhibit a nano-columnar morphology without a boundary phase. The authors argued that the B deficiency is accommodated by the formation of Ti-rich planar defects [32]. For deposition of TiB_2 using HiPIMS, Bakhit *et al.* [30] studying the effect of pulse length variations, and later Hellgren *et al.* [36] studying pressure and temperatures variations, suggested that the 32 % larger ionization potential of B (8.30 eV) compared to Ti (6.28 eV) [37] leads to a larger fraction of ionized Ti (compared to B) in the deposition flux guided towards the substrate by (stray) magnetic fields originating from the type II magnetrons, ultimately causing a reduction in B/Ti ratio.

The application of TiB_x coatings in ambient air is usually confined to temperatures below 400 °C [38–41]. Recently, Dorri *et al.* [42] observed oxide scale thicknesses of 100 ± 7 nm and 193 ± 10 nm after 12 and 3 h of oxidation at 300 and 400 °C, respectively, for initially 4 μm thick, DCMS deposited $TiB_{2.5}$ coatings. Interestingly, different oxidation products have been reported in the literature for TiB_x: Dorri *et al.* [42] reported the formation of highly B-deficient anatase/rutile-TiO_2 oxide scales at 500 and 600 °C and rutile-TiO_2 oxide scales at 700 °C. In contrast, Koh *et al.* [43] observed the formation of rutile-TiO_2 and glassy B_2O_3 as oxidation products of hot-pressed bulk TiB_2, at temperatures between 800 °C and 1000 °C, while at 1200 °C, a 100 μm thick rutile-TiO_2 scale formed after oxidation for 2 h. Cai *et al.* [44] investigated the oxidation behavior of arc melted bulk TiB_2 at 400–800 °C and reported the mixture of amorphous B_2O_3 and crystalline TiO_2 as the oxidation products. They reported an oxide scale thickness of ~ 5 μm for 0.5 h at 800 °C [44]. In another recent study, Thörnberg *et al.* [34] reported that a B-deficient HiPIMS deposited $TiB_{1.43}$ coating exhibits 2.9 ± 1.5 nm/h only 15 % of the oxidation rate of DCMS deposited $TiB_{2.70}$ coating at 400 °C for up to 48 h. The substantially lower oxidation rate of the B-deficient, $TiB_{1.43}$ coating, was ascribed to the absence of the B-rich tissue phase. The authors argued, based on [45], that the formation and subsequent evaporation of B_2O_3 observed during oxidation of B-rich thin films leads to the formation of porosity, more exposure to oxygen, and subsequently aggravation of oxidation [34]. The formation of a porous scale on B-rich thin films was also observed in other studies and explained by the hygroscopic characteristic of B_2O_3 which has a high tendency to form volatile boric acid (H_mBO_n (g)) in the vicinity of water vapor [34,42,46]. From the discussion above, it can be learned that the oxidation behavior of TiB_x is affected by the B/M ratio and that the oxidation products formed vary depending on oxidation temperature, oxidation time as well as oxidation ambient (for example partial pressure of water).

An improved oxidation behavior of TiB_x by Al addition has been reported by Bakhit *et al.* [45] where the oxidation resistance of co-sputtered (Al-HiPIMS/ TiB_2-DCMS) $(Ti_{0.68}Al_{0.32})B_{1.35}$ $(Ti_{0.29}Al_{0.14}B_{0.57})$ and DCMS deposited $TiB_{2.4}$ films was compared. It was shown that after oxidation for 0.5 h at 800 °C, the oxide scale thicknesses of the $(Ti_{0.68}Al_{0.32})B_{1.35}$ $(Ti_{0.29}Al_{0.14}B_{0.57})$ and $TiB_{2.4}$ films were ~ 470 and ~ 1900 nm, respectively. The authors suggested that the superior oxidation resistance of understoichiometric $(Ti_{0.68}Al_{0.32})B_{1.35}$ $(Ti_{0.29}Al_{0.14}B_{0.57})$ compared to the overstoichiometric $TiB_{2.4}$ could be explained by the formation of a dense, Al-containing, protective scale, whereas during oxidation of $TiB_{2.4}$, the volatile reaction product, B_2O_3, led to the formation of a Ti-rich porous oxide scale that grew significantly faster [45]. In another study, Thörnberg *et al.* [47] explored the oxidation resistance of $(Ti_{0.9}Al_{0.1})B_y$ coatings produced from a segmented AlB_2-TiB_2 target using HiPIMS for $y = 1.3–1.4$ and DCMS for $y = 1.9$. The oxidation experiments were performed at 600 °C for 1 to 10 h. After 10 h, the scale thickness on $(Ti_{0.9}Al_{0.1})B_{1.3}$, $(Ti_{0.39}Al_{0.04}B_{0.56})$, was 140 nm, while a 320 nm thick oxide scale formed on $(Ti_{0.9}Al_{0.1})B_{1.9}$, $(Ti_{0.31}Al_{0.03}B_{0.65})$ [47]. For comparison, oxidation of the DCMS deposited $TiB_{2.5}$ at the same temperature resulted in a similar scale thickness of ~ 310 nm already after 3 h [42]. The enhancement of oxidation resistance of $(Ti_{0.9}Al_{0.1})B_y$ compared to $TiB_{2.5}$ was attributed to the addition of 3.4 to 4.3 at.% of Al and the formation of a mixed Al_2O_3-TiO_2 scale instead of a TiO_2-containing scale. However, it is evident that the oxidation behavior comparison between the studies of Thörnberg *et al.* [47] and Dorri *et al.* [42] is affected by both the Al addition to TiB_x and the B/M ratio, as the presence of a B-rich tissue phase has an adverse effect on the oxidation behavior. Recently, we investigated the oxidation resistance of $(Ti_{0.35}Al_{0.65})B_y$ with $y = 1.7$, 2.0, and 2.4 coatings at 700 °C for 8 h. In this systematic investigation of the B/M ratio effect on the oxidation behavior, superior oxidation resistance of $(Ti_{0.35}Al_{0.65})B_{2.0}$ $(Ti_{0.12}Al_{0.21}B_{0.67})$ with 39 ± 7 nm oxide scale thickness, compared to $(Ti_{0.34}Al_{0.66})B_{2.4}$ $(Ti_{0.10}Al_{0.19}B_{0.71})$ with 204 ± 16 nm oxide scale thickness was observed and attributed to be due to the formation of a dense Al-containing oxide scale compared to the porous Ti-rich oxide scale formed on B-rich coating [48].

Incorporation of Al can also impact the mechanical properties of TiB_2 since density functional theory (DFT) predictions exhibited a 60 % decrease in elastic modulus from 580 GPa for TiB_2 to 250 GPa for AlB_2 [12]. Mockute *et al.* [49] investigated the structural and mechanical properties of $Ti_{1-x}Al_xB_{2+y}$ deposited by magnetron sputtering from AlB_2 and TiB_2 targets with $0.30 \leq x \leq 0.66$ and $0.07 \leq y \leq 1.22$. The indentation modulus was reported from 278 GPa for Ti-rich to 106 GPa for the Al-rich films. Stüber *et al.* [50] studied the structural and mechanical properties of near stoichiometric $Ti_{1-x}Al_xB_{2+y}$ deposited by magnetron sputtering from Al and TiB_2 targets with $0.10 \leq x \leq 0.16$ and $0.0 \leq y \leq 0.22$ and reported elastic modulus from 480 to 520 GPa. Nedfors *et al.* [51] studied the effect of Ti/(Al+Ti) ratio on the mechanical properties of DCMS deposited $(Ti_{1-x}Al_x)B_y$ and reported the elastic modulus of ~ 460, 391, 311 and 250 GPa, for $(Ti_{0.84}Al_{0.16})B_{2.8}$ $(Ti_{0.22}Al_{0.04}B_{0.74})$, $(Ti_{0.56}Al_{0.44})B_{2.25}$ $(Ti_{0.17}Al_{0.14}B_{0.69})$, $(Ti_{0.35}Al_{0.65})B_{1.98}$ $(Ti_{0.12}Al_{0.22}B_{0.66})$, and $(Ti_{0.15}Al_{0.85})B_{1.77}$ $(Ti_{0.05}Al_{0.31}B_{0.64})$, respectively, in spite of the variation of B/(Al+Ti) ratio from over stoichiometric for Ti-rich coatings to under stoichiometric for Al-rich compositions. The deviation of experimental values from theory obtained by interpolation of DFT predictions from [51] resulted in —13, —10, —16, and —18 %, respectively. This deviation was attributed mainly to the B off stoichiometric variation, namely excessive B, or Al, segregated at grain boundaries [51], showing that the mechanical properties were not only influenced by controlled increase in Al concentration but concurrently were affected by uncontrollable B/M ratios. In our previous systematic study on $(Ti_{0.35}Al_{0.65})B_y$ with $y = 1.7$, 2.0 and 2.4 coatings, it was shown that the mechanical properties are affected by the B/M ratio as a reduction in elastic modulus from 395 ± 12 GPa for $(Ti_{0.35}Al_{0.65})B_{2.0}$ $(Ti_{0.12}Al_{0.21}B_{0.67})$ to 330 ± 9 GPa for $(Ti_{0.34}Al_{0.66})B_{2.4}$ $(Ti_{0.10}Al_{0.19}B_{0.70})$ was measured and attributed to the presence of B-rich tissue phase [48].

Hence, from the above discussion, it is evident that at least two parameters define the oxidation behavior and mechanical properties, (a) Al concentration and (b) B/M ratio. Furthermore, it is evident in the published literature that, the Al concentration induced oxidation behavior improvement and mechanical properties alteration are also affected by the B/M ratio, which could not be controlled and hence varied as the Al concentration was varied systematically. Hence, previously, the causality between Al additions and oxidation behavior and mechanical properties changes were blurred by the B/M ratio which could not be controlled systematically.

To unravel the – unblurred – causality between Al concentration and oxidation behavior as well as mechanical properties variations, we utilize a previously developed methodology allowing for controlled

Table 1
Deposition parameters for diboride coatings.

Film composition (ERDA)	$Ti_{1-z}Al_z$ targets	Ti/Al power density [W/cm^2]	B power density [W/cm^2]	Deposition duration [min]	Deposition rate [nm/min]
$Ti_{0.29}Al_{0.04}B_{0.67}$	$Ti_{0.9}Al_{0.1}$	2.5	8.5	180	6.5
$Ti_{0.18}Al_{0.15}B_{0.67}$	$Ti_{0.6}Al_{0.4}$	1.5	8	210	6.2
$Ti_{0.12}Al_{0.21}B_{0.67}$	$Ti_{0.4}Al_{0.6}$	2	8.5	180	7.2
$Ti_{0.05}Al_{0.28}B_{0.67}$	$Ti_{0.2}Al_{0.8}$	1.25	9.25	180	7.0

variations of the B/M ratio [48] to study the effect of Al additions in stoichiometric (B/M = 2) $Ti_{0.33-x}Al_xB_{0.67}$ coatings with x = 0.04, 0.15, 0.21, and 0.28 for the first time. Moreover, we compare the oxidation behavior to cathodic arc deposited $Ti_{0.27}Al_{0.21}N_{0.52}$ and $Ti_{0.18}Al_{0.31}N_{0.51}$ coatings containing 21 and 31 at.% of Al, respectively, similar to the here investigated diborides with Al concentrations of 21 and 28 at.%.

2. Experimental details

$Ti_{0.33-x}Al_xB_{0.67}$ coatings were synthesized in a vacuum growth system by magnetron sputtering. The two 2-inch B targets, with a purity of 99.9 % (MaTecK, Germany), were sputtered with a radio frequency (RF) power supply (13.56 MHz). One 2-inch $Ti_{1-z}Al_z$, with z = 0.1, 0.4, 0.6, and 0.8, powder-metallurgical target (Plansee Composite Materials GmbH, Germany) was operated at different direct current (DC) power densities as indicated in Table 1 to obtain an Al concentration range variation, while maintaining the B/M stoichiometric. The base pressure was less than 1×10^{-4} Pa. α-Al_2O_3 (0001) substrates were placed at a 10 cm distance from the targets. The working gas was Ar (99.9999 % purity) with a pressure of 0.6 Pa. The substrates were heated to a temperature of 400 °C, rotated during deposition with a speed of 15 rpm, and kept at floating potential. The deposition time was adjusted to keep the deposition rate between 6.2 and 7.2 nm/min. The venting temperature was < 50 °C to minimize surface chemistry modifications by atmosphere exposure [52]. The deposition parameters, including the metal target composition and the power densities applied to the targets, are summarized in Table 1. For the calculation of the power density, the whole surface area of a target (2-inch) was considered.

An industrial deposition chamber, Ingenia P3e™, made by Oerlikon Balzers, was employed to grow single-phase cubic (Ti,Al)N coatings using cathodic arc deposition. A cylindrical sample holder was used to mount the 10 × 10 mm α-Al_2O_3 substrates, which were etched in an Ar/H_2 atmosphere at a base pressure of < 3×10^{-4} Pa. To synthesize $Ti_{0.27}Al_{0.21}N_{0.52}$ and $Ti_{0.18}Al_{0.31}N_{0.51}$ coatings, TiAl alloy targets with 50 and 67 at.% of Al were employed and the current and voltage at the targets were 177 and 121 A and 32.0 ± 1.4 and 21.8 ± 0.2 V with corresponding deposition rates of 29.7 and 18.2 nm/min, respectively. The coatings were deposited in nitrogen pressures of 3.2 and 3.5 Pa and at substrate temperatures of 450 and 480 °C, respectively, using two-fold substrate rotation at a speed of 3 rpm with a DC substrate bias potential of −40 V. The coating thicknesses were approximately 1.3 and 1.8 μm. The venting temperature was < 100 °C.

A GERO tube furnace (SR70–200/12) was employed for oxidation experiments in ambient air at 700, 800, and 900 °C for durations of 1, 4, and 8 h. The furnace was pre-heated to the desired oxidation temperatures and the as-deposited samples were placed in an Al_2O_3 crucible, while a Ni/Ni-Cr thermocouple was utilized to measure the temperature. The samples were immediately removed from the furnace after oxidation.

The as-deposited and oxidized coatings were characterized with a Bruker AXS D8 Discover General Area Diffraction Detection System. The Cu X-ray source (λ = 0.154 nm) was operated at a voltage and current of 40 kV and 40 mA, respectively, and the incidence angle was fixed at 15°. A profile fitting-based software (TOPAS V.3) with a pseudo-Voigt II function was used for peak fitting. Lattice parameters were determined using the CellCalc software V.2.10.

Time-of-flight elastic recoil detection analysis (ToF-ERDA) was done at the Tandem Laboratory of Uppsala University [53] to obtain depth profiles of the film composition. Recoils were created with a primary $^{127}I^{8+}$ ion beam at 36 MeV [53]. The incidence and exit angles were 22.5° with respect to the specimen surface, while the angle between the primary ion beam and the detector telescope was 45°. The detection telescope consisted of thin carbon foils for measuring the time-of-flight [54] as well as a segmented gas detector [55] for measuring the recoil energy, hence, time-energy coincidence spectra were recorded. The as-deposited $Ti_{0.12}Al_{0.21}B_{0.67}$ and $Ti_{0.18}Al_{0.31}N_{0.51}$ coatings were characterized in our previous work with a maximum total measurement uncertainty of 5 % of the deduced B and N concentrations as well as aliquot fractions thereof for the metals Ti and Al [48].

To analyze the microstructure of the coatings in the as-deposited and oxidized states by scanning transmission electron microscopy (STEM), thin lamellae were prepared by focused ion beam techniques using a FEI Helios Nanolab 660i dual-beam microscope at 30 kV voltage and a current of 50 pA. To analyze the relationship between coating composition and oxidation behavior, the combination of high angle annular dark field (HAADF) imaging and energy dispersive X-ray spectroscopy (EDX) line scans were used. EDX spectra were acquired at 10 kV acceleration voltage and 1.6 nA current. EDX mapping was conducted in a Titan Themis 200 G3 equipped with a SuperX EDX detector (Thermo Fisher Scientific) at an acceleration voltage of 200 kV.

Elastic modulus and hardness values of the as-deposited coatings were measured by nanoindentation using a Hysitron TI-900 TriboIndenter. The indentations were carried out using a Berkovich geometry diamond tip with a 100 nm radius. To minimize the substrate influence, the contact depths were set to < 10 % with respect to the film thickness and by applying different loads from 2 to 5 mN. A maximum load of 3 mN was chosen for diborides resulting in a maximum penetration depth of 85 nm. For larger loads, the measured data was affected by the substrate. The indentation modulus was obtained from the unloading part of the load-displacement curves according to the method of Oliver and Pharr [56]. To obtain the elastic modulus for diborides from the reduced elastic modulus, calculated Poisson's ratio values of 0.134, 0.183, 0.213, and 0.240 for $Ti_{0.33-x}Al_xB_{0.67}$ with x = 0.04, 0.15, 0.21, and 0.28 compositions, respectively, were used. Throughout the discussion in this paper, we cite the chemical composition measured in at.%. While citing chemical compositions utilizing stoichiometric factors from literature, we add the at.% notation in brackets for the convenience of the reader.

3. Computational details

Ab initio calculations were performed in the framework of DFT [57, 58] as implemented in the Vienna *Ab initio* Simulation Package (VASP) [59,60]. A plane-wave basis set with the generalized gradient approximation (GGA) in the Perdew-Burke-Ernzerhof (PBE) parameterization [61] to describe the exchange-correction effects was applied. As the cutoff energy, 500 eV was chosen based on the results of convergence test runs on a selection of configurations. The cutoff for the forces was set in accordance with previous publications for similar systems i.e. [62]. The first Brillouin zone was sampled with a 6 × 6 × 6 K-point mesh centered at the Γ point. The calculations were considered converged with an energy difference of 10^{-5} eV and atomic forces lower than 10^{-2} eV/Å. For the calculations, 4 × 4 × 4 supercells containing 192 atoms with the hexagonal AlB_2 structure were created. The sublattices were populated using the special quasi-random structure (SQS) method [63]. The stiffness tensor was obtained with the strain-stress method [64]. The Poisson's ratio along with other elastic properties (Young's, shear and bulk modulus) were calculated in the form of the full stiffness tensor (C_{ij}), from which the elastic modulus was derived with the Voigt-Reuss-Hill scheme [65].

Table 2
Chemical composition of coatings obtained by ERDA.

Ti [at.%]	Al [at.%]	B [at.%]	N [at.%]	Nomenclature
29.1 ± 2.9	4.2 ± 0.4	66.7 ± 3.3	–	$Ti_{0.29}Al_{0.04}B_{0.67}$
18.1 ± 1.8	15.5 ± 1.5	66.4 ± 3.3	–	$Ti_{0.18}Al_{0.15}B_{0.67}$
11.6 ± 1.2	21.4 ± 2.2	67.0 ± 3.4	–	$Ti_{0.12}Al_{0.21}B_{0.67}$
5.4 ± 0.5	27.7 ± 2.8	66.9 ± 3.3	–	$Ti_{0.05}Al_{0.28}B_{0.67}$
27.2 ± 1.5	21.0 ± 1.1	–	51.8 ± 2.6	$Ti_{0.27}Al_{0.21}N_{0.52}$
18.1 ± 1.0	30.9 ± 1.6	–	51.0 ± 2.6	$Ti_{0.18}Al_{0.31}N_{0.51}$

4. Results and discussion

The chemical compositions measured by ERDA as well as the corresponding chemical formulae of the coatings investigated in this work are displayed in Table 2. The concentration of Al increases from 4.2 via 15.5 and 21.4 to 27.7 at.%. Meanwhile, the B concentration ranges from 66.4 to 67.0 at.%. Hence, considering the measurement uncertainties, all diboride coatings depicted in Table 2, are stoichiometric. For simplicity, the coating compositions are referred to as $Ti_{0.29}Al_{0.04}B_{0.67}$, $Ti_{0.18}Al_{0.15}B_{0.67}$, $Ti_{0.12}Al_{0.21}B_{0.67}$, and $Ti_{0.05}Al_{0.28}B_{0.67}$ in the following discussion. The oxygen concentrations varied between 1.4 to 3.0 at.%. Oxygen incorporation occurs likely due to reactions with residual gas during the growth process [66] and/or reactions during exposure to the surrounding atmosphere after growth [52].

The chemical composition of the nitride coatings is also displayed in Table 2. The coatings are N over stoichiometric with Al concentrations of 21.0 and 30.9 at.%. The sum of C and O impurities is < 1 at.%. In the following discussion, the nitride coatings are referred to as $Ti_{0.27}Al_{0.21}N_{0.52}$ and $Ti_{0.18}Al_{0.31}N_{0.51}$.

The phase formation of the coatings grown on sapphire (0001) was studied by XRD and the diffractograms are presented in Fig. 1. The TiB_2 and AlB_2 reference lines, based on the PDF cards 00–035–0741 and 00–008–0216, are represented by square and circle markers, respectively. Independent of composition, all coatings form a polycrystalline

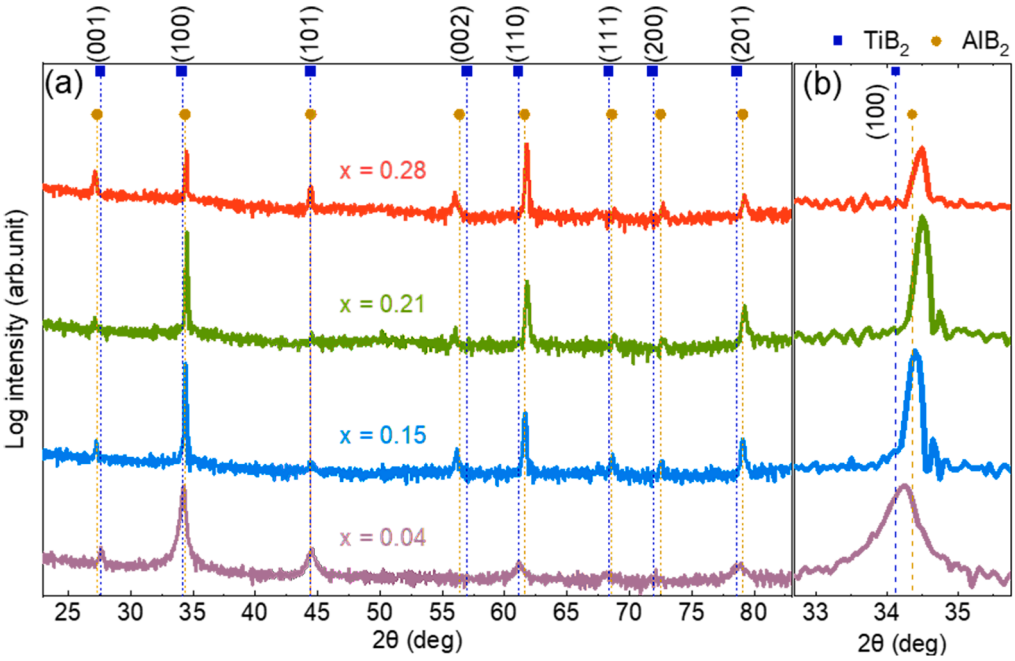


Fig. 1. Diffraction patterns of (a) as-deposited $Ti_{0.33-x}Al_x B_{0.67}$ coatings (b) zoom in for (100) reflection.

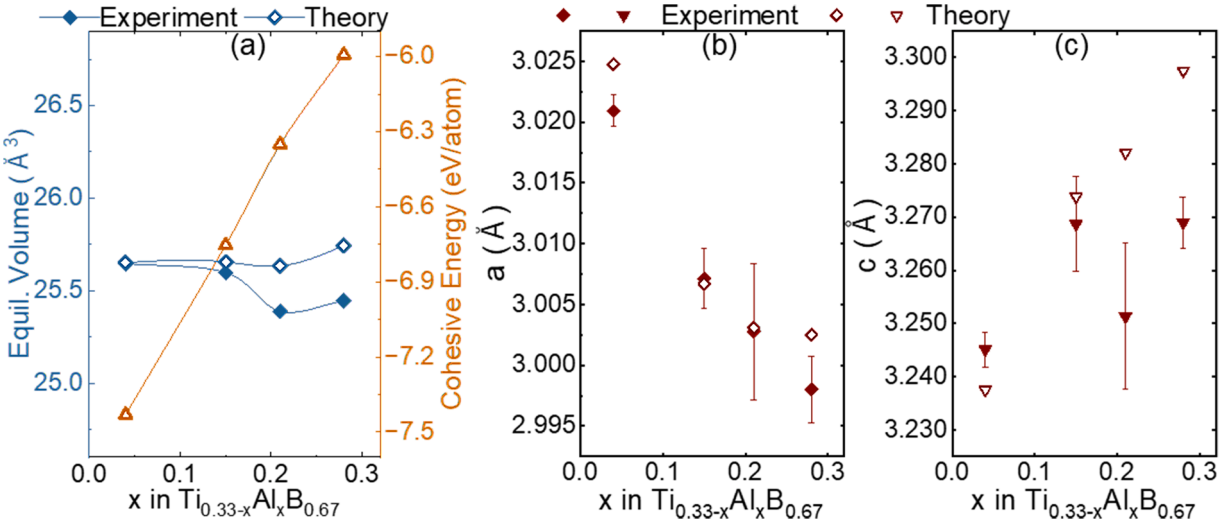


Fig. 2. Experimental and theoretical values of unit cell volume and cohesive energy (a), lattice parameter *a* (b), and lattice parameter *c* (c) of diborides.

Table 3
Experimental and theoretical values of lattice parameters and unit cell volume and cohesive energy of diborides.

	Exp.			DFT			Cohesive energy (eV/atom)
	a (Å)	c (Å)	V (Å^3)	a (Å)	c (Å)	V (Å^3)	
TiB_2	3.030	3.223	25.683	3.032	3.229	25.707	−7.691
$Ti_{0.29}Al_{0.04}B_{0.67}$	3.021	3.245	25.646	3.025	3.238	25.651	−7.430
$Ti_{0.18}Al_{0.15}B_{0.67}$	3.007	3.269	25.598	3.009	3.272	25.655	−6.753
$Ti_{0.12}Al_{0.21}B_{0.67}$	3.003	3.251	25.388	3.003	3.282	25.634	−6.351
$Ti_{0.05}Al_{0.28}B_{0.67}$	2.998	3.269	25.445	3.003	3.298	25.744	−5.993
AlB_2	3.009	3.262	25.577	3.007	3.292	25.778	−5.711

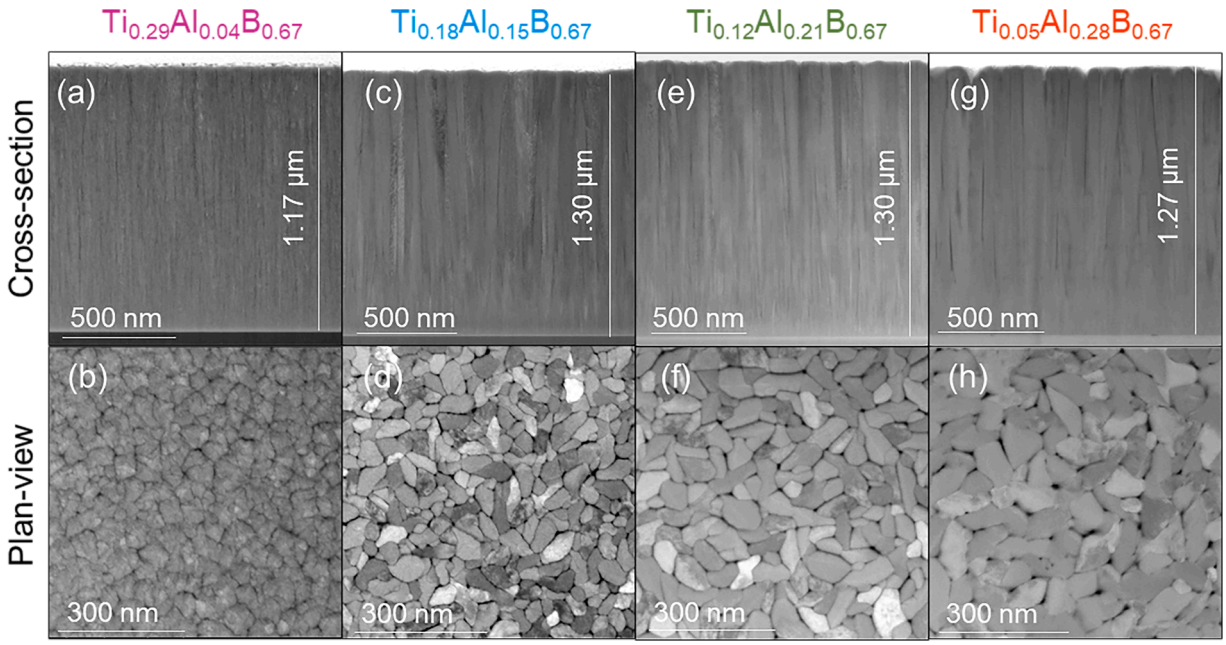


Fig. 3. Cross-sectional and plan-view STEM images of as-deposited, (a) and (b) $Ti_{0.29}Al_{0.04}B_{0.67}$, (c) and (d) $Ti_{0.18}Al_{0.15}B_{0.67}$, (e) and (f) $Ti_{0.12}Al_{0.21}B_{0.67}$, and (g) and (h) $Ti_{0.05}Al_{0.28}B_{0.67}$ coatings in HAADF mode.

single-phase hexagonal solid solution. As the Al concentration is increased, the measured peak positions exhibit a shift towards the AlB_2 positions, indicating the substitution of Ti (atomic radius = 1.470 Å) by Al (atomic radius = 1.431 Å) [67], see Fig. 1(b) displaying a high-resolution scan of the (100) peak shift.

The experimental and calculated values of the lattice parameters converted into volume unit cell and calculated cohesive energy are shown and compared in Fig. 2 and Table 3. In general, when the Al

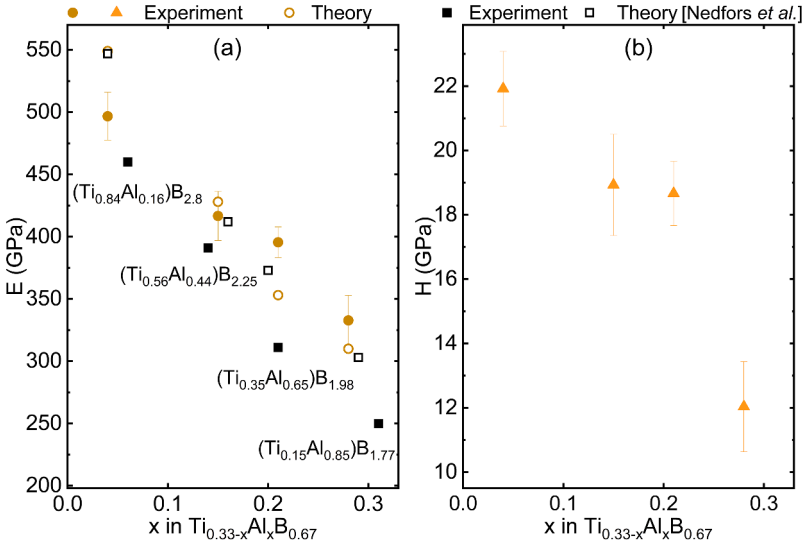


Fig. 4. Experimental and predicted (a) elastic modulus data with values from [51] and (b) hardness as a function of Al concentration for as-deposited coatings.

concentration is increased, the lattice constant a tends to decrease, consistent with the DFT predictions, while the lattice constant c does not exhibit a clear trend, which contrasts with the DFT predicted values, showing an upward trend. The PDF cards 00-035-0741 and 00-008-0216 specify experimental lattice parameters and unit cell volumes for TiB_2 (25.683 Å^3) and AlB_2 (25.577 Å^3). Hence, the absolute and relative changes in unit cell volume as Ti (atomic radius = 1.470 Å) is substituted by Al (atomic radius = 1.431 Å) [67] are 0.106 Å^3 and 0.41 %, respectively. The Al concentration induced change of unit cell volume ($\leq$ 0.78 %) and lattice parameter ($\leq$ 0.76 %) in the range studied here (4 to 28 at.%), corresponds to a 2 theta variation of $\geq$ 0.2 ° and is hence resolvable by XRD. Moreover, the measured lattice parameters of $Ti_{0.29}Al_{0.04}B_{0.67}$, and $Ti_{0.18}Al_{0.15}B_{0.67}$ (see Table 3) exhibit deviations of up to a maximum of 0.23 % from the calculated DFT values. This deviation increases for $Ti_{0.12}Al_{0.21}B_{0.67}$ and $Ti_{0.05}Al_{0.28}B_{0.67}$ to a maximum of 0.94 %. Hence, the here observed deviations between measured and predicted lattice parameters are in very good agreement as, according to Paier *et al.* [68], deviations between experimental and theoretical lattice parameters of up to 2 % have to be expected for the here employed exchange correlation functionals. As the Al concentration is increased from 4 to 28 at.%, cohesive energy values increase from —7.7 to —6.0 eV/atom, implying an Al concentration induced bond weakening.

In Fig. 3, cross-sectional and plan-view STEM images of as-deposited diboride coatings are shown. All coatings exhibit a morphology with fine columns near the substrate, which gradually broaden along the growth direction. It can be observed that by increasing the Al concentration, the diameter of the columns increases, as witnessed by the plan view STEM images, see Fig. 3(b), (d), (f), and (h), while voids at grain boundaries and triple junctions are visible for all coatings. The void volume increases with increasing Al concentration from ~ 5 nm for 4 at.% to ~ 20 nm for 28 at.% of Al.

Fig. 4 displays the Al concentration induced changes in elastic modulus and hardness values. With increasing Al concentration in $Ti_{0.33-x}Al_xB_{0.67}$, the elastic modulus decreases in a close to linear fashion from 496 ± 19 for the coating containing 4 at.% of Al to 332 ± 20 for an Al concentration of 28 at.%. This corresponds to a reduction of ~ 7 GPa per at.% of Al incorporated. This elastic modulus reduction can be rationalized by considering the Al concentration induced bond weakening as witnessed by the concomitant cohesive energy reduction of 19 %, from —7.430 (eV/atm) for 4 at.% to —5.993 (eV/atm) for 28 at.% of Al (Table 3). Since here the B/M ratios, considering the error of the measurement, are equal to 2, the changes in mechanical properties can be ascribed to changes in Al concentration as well as to the presence of voids at column boundaries and triple junctions, see Fig. 3.

Consistent with the experiment, DFT calculations predict a nearly linear, and hence Vegard like, decrease in elastic modulus for the stoichiometric $Ti_{0.33-x}Al_xB_{0.67}$ solid solution between TiB_2 (E = 586 GPa) and AlB_2 (E = 234 GPa). As the maximum deviation between the experimental and theoretical values in this study is $\leq$ 12 %, the agreement according to Eriksson *et al.* [69] is within the expected 15 % range for the functionals employed here. As the magnitude of the here measured elastic modulus may also be affected by morphology [48], compressive stress [70] as well as by defects [71], it is reasonable to assume that these contributions are small as the agreement between theory and experiment is very good. Different experimental values of elastic modulus for apparently identical coating compositions have been reported in the literature, and these reported discrepancies could be attributed to differences in the B quantification technique [72], compressive stress [70], ion kinetic energy, and the deposition route [73]. The diboride coatings were investigated regarding residual stress employing the $\sin^2\psi$ method. The calculated stresses, however, were inconclusive due to the film texture and the comparatively low diffracted intensity.

The measured hardness as a function of Al concentration is presented in Fig. 4(b) exhibiting a similar descending trend as the elastic modulus. In Fig. 4(b), the coating with 4 at.% of Al shows 22 ± 1 GPa, the highest

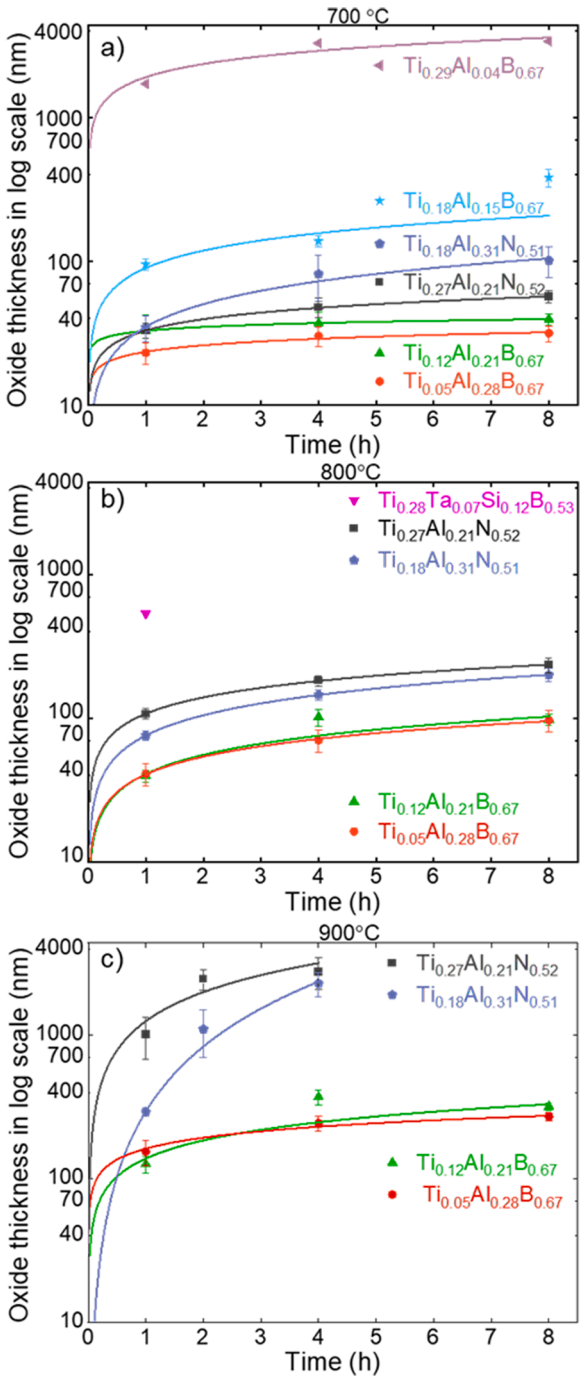


Fig. 5. The oxide scale thickness of diborides and nitrides as a function of oxidation time at (a) 700 °C containing data from [48], (b) 800 °C containing data from [76] and (c) 900 °C.

hardness. The coatings with 15 and 21 at.% of Al exhibit similar values of 19 ± 2 and 19 ± 1 GPa, respectively, while the coating containing 28 at.% of Al shows 12 ± 1 GPa, the lowest hardness. Nedfors *et al.* [51] reported an Al concentration induced reduction of hardness from ~ 38 ± 2, via 29 ± 2 and 25 ± 2 to 18 ± 2 GPa for $(Ti_{0.84}Al_{0.16})B_{2.8}$ $(Ti_{0.22}Al_{0.04}B_{0.74})$, $(Ti_{0.56}Al_{0.44})B_{2.25}$ $(Ti_{0.17}Al_{0.14}B_{0.69})$, $(Ti_{0.35}Al_{0.65})B_{1.98}$ $(Ti_{0.12}Al_{0.22}B_{0.66})$, and $(Ti_{0.15}Al_{0.85})B_{1.77}$ $(Ti_{0.05}Al_{0.31}B_{0.64})$, respectively. It was proposed that the formation of the B-rich tissue phase and (001) preferred orientation influenced the measured hardness values [51]. According to Mayrhofer *et al.* [2], the high hardness of B-rich thin films is caused by the presence of a B-rich tissue phase at grain boundaries and a fine-grained microstructure which impedes

plastic deformation [2]. Recently Fuger *et al.* [74] reported an increase in hardness of > 10 GPa for DCMS-deposited TiB_z ($z = 2.07$ - 3.6) as the films exhibited a more pronounced (001) texture. Moreover, Nedfors *et al.* [51] reported that preferred orientation has a stronger impact on hardness than Ti content for $(Ti_xAl_{1-x})B_y$ with $x > 0.79$ and $y > 2.7$. Thörnberg *et al.* [47] reported the hardness values of 46 ± 1 GPa for $(Ti_{0.9}Al_{0.1})B_{1.3}$ ($Ti_{0.39}Al_{0.04}B_{0.56}$) via 29 ± 2 GPa for $(Ti_{0.6}Al_{0.4})B_{1.3}$ ($Ti_{0.26}Al_{0.18}B_{0.56}$) and 23 ± 1 GPa for $(Ti_{0.3}Al_{0.7})B_{1.3}$ ($Ti_{0.13}Al_{0.30}B_{0.56}$). The decrease in hardness values of $(Ti_{1-x}Al_x)B_{1.3}$ was attributed to an increase in Al concentration from 4.3 to 30.4 at.%. Moreover the reported decline in hardness of $(Ti_{0.9}Al_{0.1})B_y$ from 46 ± 1 GPa for $y = 1.3$ ($Ti_{0.39}Al_{0.04}B_{0.56}$) to 36 ± 1 GPa for $y = 1.9$ ($Ti_{0.31}Al_{0.03}B_{0.65}$) was ascribed to B concentration alteration from 56.5 to 63.3 at.%, respectively [47]. The coatings in the present work show lower values of hardness compared to the literature values which can be rationalized as different factors such as the lack of a (001) texture [51,74], differences in residual stress state [71], underdense morphology [48,71], defect structure [71,75] and absence of B-rich tissue phase [2] are expected to affect the measured hardness values. Also, the fact that the films here were grown at floating potential while Thörnberg *et al.* [47] and Bartosik *et al.* [75] employed ion bombardment via substrate biasing is expected to be relevant in the context. It is therefore reasonable to assume that the complex interplay of the aforementioned factors is responsible for the here observed hardness differences.

Oxidation experiments were carried out to analyze the effect of the Al concentration on the oxidation of $Ti_{0.33-x}Al_xB_{0.67}$ at 700, 800, and 900 °C for 1, 4, and 8 h. Fig. 5(a), (b) and (c) compare the time-dependent oxidation behavior of borides and nitrides. The fitted lines serve as guide for the eye and the discussion related to oxidation kinetics can be found in the supplementary materials.

At 700 °C (Fig. 5(a)), the diboride coating with an Al concentration of 4 at.%, is fully oxidized after 8 h while the coatings containing 15 and 28 at.%, show oxide scale thicknesses of 382 ± 55 to 31 ± 5 nm, respectively, indicating improved oxidation resistance. At 800 °C (Fig. 5 (b)), diborides with ≥ 21 at.% of Al exhibit oxide scale thickness of ≤ 98 ± 8 nm compared to the nitrides with minimum of 200 nm.

Bahr *et al.* [76] explored the oxidation behavior of 3 to 5 μm-thick quaternary borides and reported an outstanding oxidation resistance for $Ti_{0.23}Mo_{0.07}Si_{0.16}B_{0.54}$ with oxide scale thickness of 440 nm at 1200 °C and for $Ti_{0.28}Ta_{0.07}Si_{0.12}B_{0.53}$ with 535 nm oxide scale thickness at 800 °C in ambient air after 1 h due to the formation of amorphous Si-containing oxide scales. At 700 [48], 800, and 900 °C, both nitrides investigated here, namely $Ti_{0.27}Al_{0.21}N_{0.52}$ and $Ti_{0.18}Al_{0.31}N_{0.51}$ exhibit inferior oxidation resistance compared to corresponding diborides with similar Al concentrations. For example, after 1 h at 900 °C, $Ti_{0.27}Al_{0.21}N_{0.52}$ and $Ti_{0.18}Al_{0.31}N_{0.51}$ exhibit a factor of 8.0 and 1.9 larger oxide scale thicknesses compared to diboride coatings containing 21 and 28 at.% of Al, respectively. However, at 900 °C (Fig. 5(c)) $Ti_{0.27}Al_{0.21}N_{0.52}$ is fully oxidized after 2 h while $Ti_{0.18}Al_{0.31}N_{0.51}$ is fully oxidized after 4 h, see Figure S 1 and Figure S 2 in supplementary materials. While the improvement in oxidation resistance observed here is due to the addition of Al to TiB_z which appears – at first glance – to be consistent with the literature, the effect of Al incorporation into stoichiometric - compounds has not been reported yet. The here presented data, exclusively from coatings with a B/M ratio of 2, allow - for the first time - for unambiguous quantification of the Al incorporation effect on the oxidation behavior as deviations from stoichiometry as present in all literature data sets [45,47] were avoided. The substantial enhancement in oxidation resistance of the diboride coatings with Al ≥ 21 at.% and the significantly higher oxidation rates for Al ≤ 15 at.%, imply a strong Al concentration dependent oxidation behavior in the here studied time and temperature range.

To elucidate the Al concentration dependent oxidation behavior as a function of time and temperature in greater detail, the remaining thickness of the coating after oxidation d_r is compared to the thickness of the as-deposited diboride coatings d_i with the average thickness of 1.26

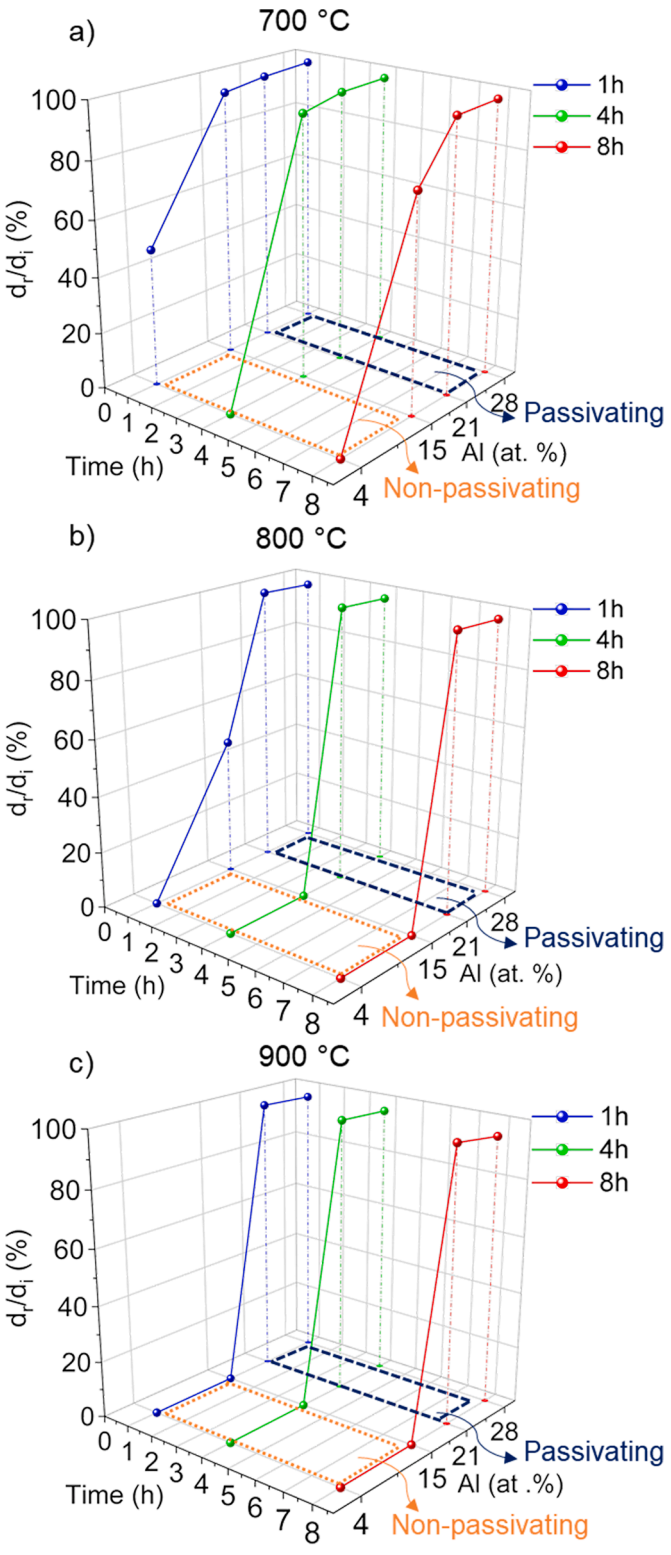


Fig. 6. The remaining film thickness/initial thickness (d_r/d_i) as a function of Al concentration in at.% after oxidation at (a) 700 °C, (b) 800 °C, and (c) 900 °C for 1, 4 and 8 h.

Table 4
The coating thickness in the as-deposited state (d_i), the remaining coating thickness after oxidation (d_r), the difference between the coating thickness prior to oxidation and the remaining coating thickness ($d_i - d_r$) and R ratio data for all oxidation conditions.

	d_i (nm)	Oxidation time (h)	d_r (nm)						$d_i - d_r$ (nm)			$R = \left(\frac{d_r}{d_i}\right) \times 100$		
			700 °C	std	800 °C	std	900 °C	std	700 °C	800 °C	900 °C	700 °C	800 °C	900 °C
$Ti_{0.29}Al_{0.04}B_{0.67}$	1170	1	570	110	0		0		600	1170	1170	49	0	0
$Ti_{0.18}Al_{0.15}B_{0.67}$	1300	1	1232	15	628	162	0		68	672	1300	95	48	0
$Ti_{0.12}Al_{0.21}B_{0.67}$	1300	1	1268	16	1262	14	1250	21	32	38	50	97	97	97
$Ti_{0.05}Al_{0.28}B_{0.67}$	1270	1	1239	35	1228	27	1218	35	31	42	52	98	97	96
$Ti_{0.29}Al_{0.04}B_{0.67}$	1170	4	0		0		0		1170	1170	1170	0.0	0	0
$Ti_{0.18}Al_{0.15}B_{0.67}$	1300	4	1213	21	0		0		87	1300	1300	93	0	0
$Ti_{0.12}Al_{0.21}B_{0.67}$	1300	4	1266	18	1264	23	1261	20	34	36	39	97	97	97
$Ti_{0.05}Al_{0.28}B_{0.67}$	1270	4	1235	31	1225	34	1218	34	35	45	52	97	96	96
$Ti_{0.29}Al_{0.04}B_{0.67}$	1170	8	0		0		0		1170	1170	1170	0.0	0	0
$Ti_{0.18}Al_{0.15}B_{0.67}$	1300	8	1002	126	0		0		298	1300	1300	77	0	0
$Ti_{0.12}Al_{0.21}B_{0.67}$	1300	8	1259	29	1262	24	1260	23	41	38	40	97	97	97
$Ti_{0.05}Al_{0.28}B_{0.67}$	1270	8	1234	33	1230	35	1203	37	36	40	67	97	97	95

$\pm$ 0.05, in the ratio R, Eq. (2):

$$R = \left(\frac{d_r}{d_i}\right) \times 100 \quad (2)$$

Where, for example, an R value of 20 % indicates that 20 % of the as-deposited coating thickness remains unoxidized. The Al concentration and oxidation time induced changes in R, are displayed in Fig. 6(a) for 700 °C, in Fig. 6(b) for 800 °C, and in Fig. 6(c) for 900 °C. The coating thickness in the as-deposited state (d_i), the remaining coating thickness after oxidation (d_r), the difference between the coating thickness prior to oxidation and the remaining coating thickness ($d_i - d_r$) and R ratio data for all oxidation conditions investigated here can be found in Table 4.

For coatings containing Al $\leq$ 15 at.%, the R value decreases with increasing oxidation time for each specific Al concentration e.g., the coating with an Al concentration of 4 at.% exhibits an R value decrease from 49 % for 1 h at 700 °C to 0 % at 4 h, indicating complete oxidation, see Fig. 6(a). Contrarily, for coatings containing 21 and 28 at.% of Al, R values of 97 and 98 %, respectively, are obtained regardless of the oxidation duration. As the oxidation temperature and time are increased, see Fig. 6(b) and Fig. 6(c) the minimum R value measured for coatings with an Al concentration of $\geq$ 21 at.% is 95 %, while it is evident that it is only a question of time until the coatings containing $\leq$ 15 at.% are fully oxidized. Hence, it is evident that the time and temperature dependent oxidation behavior in the here studied parameter space is bimodal in nature: Fast oxidation is observed for coatings containing $\leq$ 15 at.%, while for Al concentrations of $\geq$ 21 at.%, slow oxide scale growth is witnessed by the remaining, unoxidized coating thicknesses within the R value comparison presented above.

To rationalize this bimodal oxidation behavior, structural characterization data of the oxidized material is discussed next: Figure S 3 and Figure S 4 (a) and (b) depict the diffractograms of as-deposited and oxidized coatings containing 4 and 15 at.% of Al. The TiO_2 and Al_2TiO_5 reference lines, based on the PDF cards 01-072-7347 and 00-046-0258, are represented by triangle and diamond markers, respectively. Evidence for the formation of crystalline Al_2TiO_5 and TiO_2 phases after oxidation for 1, 4, and 8 h at 700 and 800 °C are displayed in Figure S 3 and Figure S 4. Figure S 5 (a) and (b) illustrate the diffractograms of as-deposited and oxidized coatings containing 21 and 28 at.% of Al, respectively, after 8 h at 700, 800 and 900 °C. No evidence for the formation of crystalline oxide phases can be seen in these diffractograms, suggesting that even after oxidation at 900 °C for 8 h, the formed oxide scale is X-ray amorphous. Hence, structural analysis data obtained by XRD confirmed the bimodal oxidation behavior notion presented above, as coatings with $\leq$ 15 at.% of Al concentration form crystalline scales containing Al_2TiO_5 and TiO_2, while for coatings containing $\geq$ 21 at.% of Al the formation of X-ray amorphous scales was observed. To understand the origin of this dual-mode oxidation behavior in greater depth, spatially resolved morphological, structural, and compositional analyses of the oxide scales were performed.

Fig. 7 depicts the cross-sectional images of the oxidized coatings, obtained from STEM imaging and corresponding EDX analysis on FIB prepared lamellae after oxidation at 700, 800, and 900 °C for 8 h. The zero distance values in the EDX line scans depicted in Fig. 7 correspond to the Pt layer introduced during FIB lamellae preparation. The lamellae thicknesses were < 100 nm and the beam diameter used for the EDX line scans was approximately 50 nm. The probed volume is based on the work of Notthoff *et al.* [77] expected to be significantly larger than the volume computed from sample thickness and diameter. As a result, the resolution of the oxide/film interface analysis is limited by the probed volume.

The cross-sectional STEM images reveal that the coatings with an Al concentration $\leq$ 15 at.% form non-conformal and porous scales at 700 and 800 °C, see Fig. 7(a) and (b) as well as Figure S 6 and Figure S 7 (a) in the supplementary materials. Specifically, the coating with an Al concentration of 15 at.% exhibits a non-conformal double-layer oxide scale consisting of an Al-rich mixed (Ti and Al) outer porous layer and Ti-rich mixed (Ti and Al) nodular inner layer with a thickness of 382 $\pm$ 55 nm (Fig. 7(a)) at 700 °C. This coating is fully oxidized at 800 °C (Fig. 7(b)) exhibiting an Al-rich mixed (Ti and Al) outer porous layer and a columnar Ti-rich mixed (Ti and Al) inner oxide layer. The corresponding diffractograms, shown in Figure S 4, indicate the formation of crystalline TiO_2 and Al_2TiO_5.

All coatings with Al concentrations $\geq$ 21 at.% form a dense, single oxide scale layer containing primarily Al and O, see Fig. 7(c) to (h) and Figure S 7 in supplementary material. While the Al concentration is, compared to the as-deposited coating, enriched, the B and Ti concentrations in the scale appear to be significantly reduced. The scale thicknesses after 8 h of oxidation are 39 $\pm$ 7 nm, see Fig. 7(c), 98 $\pm$ 8 nm, see Fig. 7(d) and 319 $\pm$ 20 nm, see Fig. 7(e) at 700, 800, and 900 °C, respectively. From X-ray diffraction, no evidence supporting the formation of a crystalline oxide scale can be obtained. For the passivating coating composition, the oxygen concentration in the "remaining coating thickness" is $\leq$ 10 at% which may be attributed to the diffusion of oxygen along the grain boundary and/or oxygen uptake after lamellae preparation due to atmosphere exposure during transport while in the non-passivating coating compositions the "remaining coating thickness" is characterized by oxygen concentrations > 10 at.%. The most extreme example can be seen in Figure S 6 (a) with approximately 20 at.% of oxygen incorporated into the remaining coating."

Analyses by STEM and EDX reveal that the coatings containing $\leq$ 15 at.% of Al exhibit scales with porous morphology containing B, Ti, and Al, while the coatings with Al $\geq$ 21 at.% show dense scales consisting of

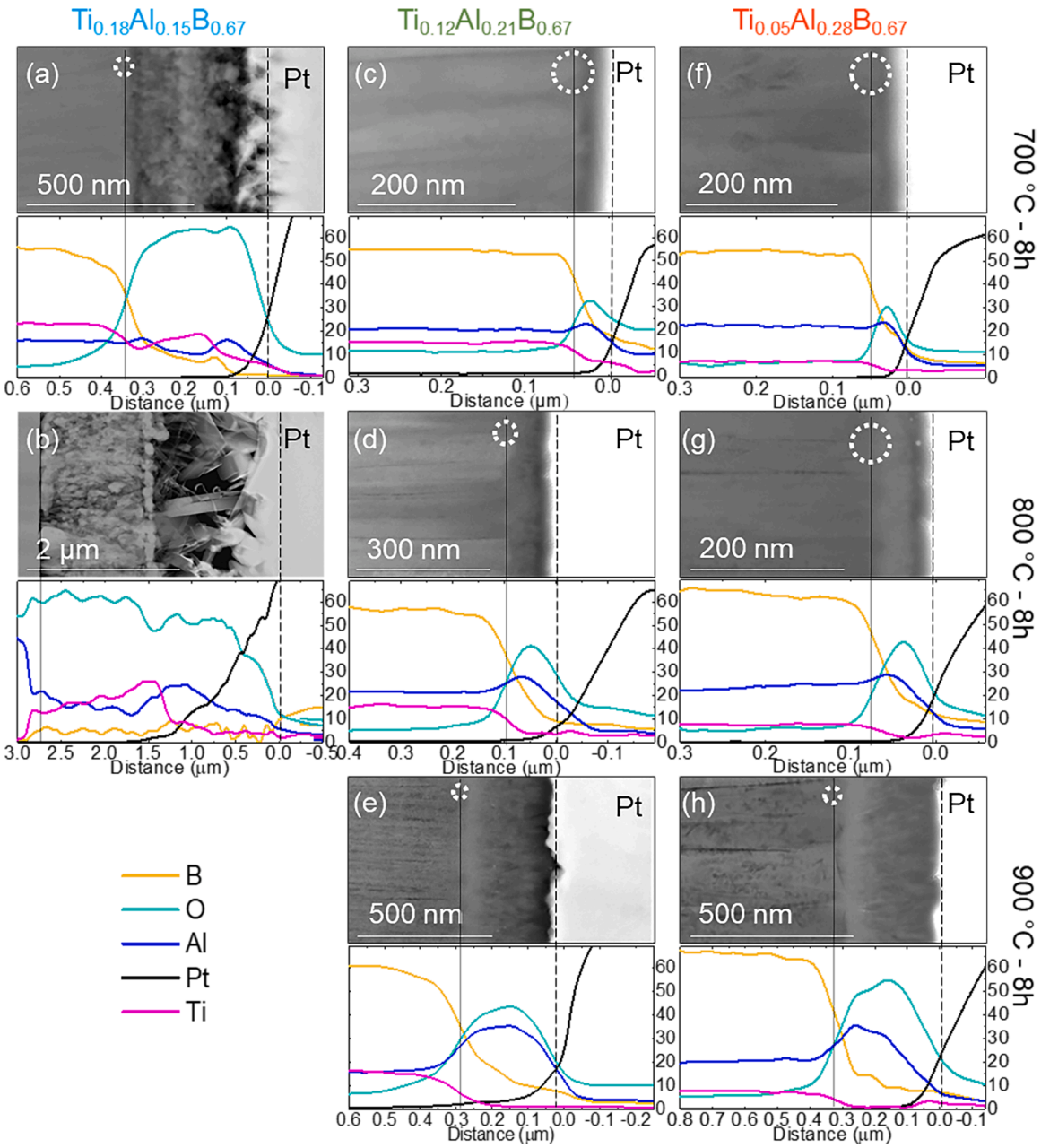


Fig. 7. Cross-sectional images and corresponding EDX line scans of oxidized $Ti_{0.18}Al_{0.15}B_{0.67}$ at (a) 700 °C and (b) 800 °C; $Ti_{0.12}Al_{0.21}B_{0.67}$ at (c) 700 °C [48], (d) 800 °C, and (e) at 900 °C; $Ti_{0.05}Al_{0.28}B_{0.67}$ at (f) 700 °C, (g) 800 °C, and (h) 900 °C, all for 8 h. The circles represent the electron beam diameter of 50 nm.

primarily Al and O, confirming the previously observed bimodality in the oxidation behavior of this material system.

To discern the disparity in oxidation behavior between coatings with Al concentrations $\leq$ 15 and $\geq$ 21 at.%, the corresponding oxide scales were investigated in terms of morphology and spatially resolved chemical composition by high-resolution STEM. To this end, the oxide scales formed on coatings with Al concentrations of 15 at.% and 28 at.% after 4 h at 700 °C were imaged in HAADF mode, and EDX elemental maps with corresponding line scans were obtained from cross-sectional FIB prepared lamellae and are shown in Fig. 8. The scale thicknesses measured on $Ti_{0.18}Al_{0.15}B_{0.67}$, see Fig. 8(a) and on $Ti_{0.05}Al_{0.28}B_{0.67}$, see Fig. 8(j) were 138 $\pm$ 13 nm and 30 $\pm$ 5 nm, respectively. For $Ti_{0.18}Al_{0.15}B_{0.67}$, a non-conformal scale with Al-rich and Ti-rich regions is evident from the EDX maps as well as from the line scan analysis compiled in Fig. 8. Although the signal from B is weak, see Fig. 8(d), the presence of $\sim$ 9 at.% B in the oxide scale was confirmed by ERDA measurements, see Figure S 8 in the supplementary materials.

On top of the coating with an Al concentration of 28 at.%, which was oxidized at identical conditions as the previously discussed coating with 15 at.% of Al, the formation of a dense scale consisting of Al and O is observed and shown in Fig. 8(k) and (l). From the high-resolution data displayed in Fig. 8(m) and (n), there is no indication for the presence of Ti in the scale while the presence of B cannot be excluded.

Hence, the analysis of the above discussed structure, morphology, and composition data augmented by spatially resolved composition data also reveals a bimodal oxidation behavior. Interestingly, the chemical composition boundaries of the dual-mode oxidation behavior are identical to the ones obtained from the discussed changes in the R ratio, reflecting the magnitude of oxidation induced changes in the remaining coating thickness. While identifying the location of the boundary between non-passivating and passivating behavior, for the here investigated time and temperature space in the Al concentration range between

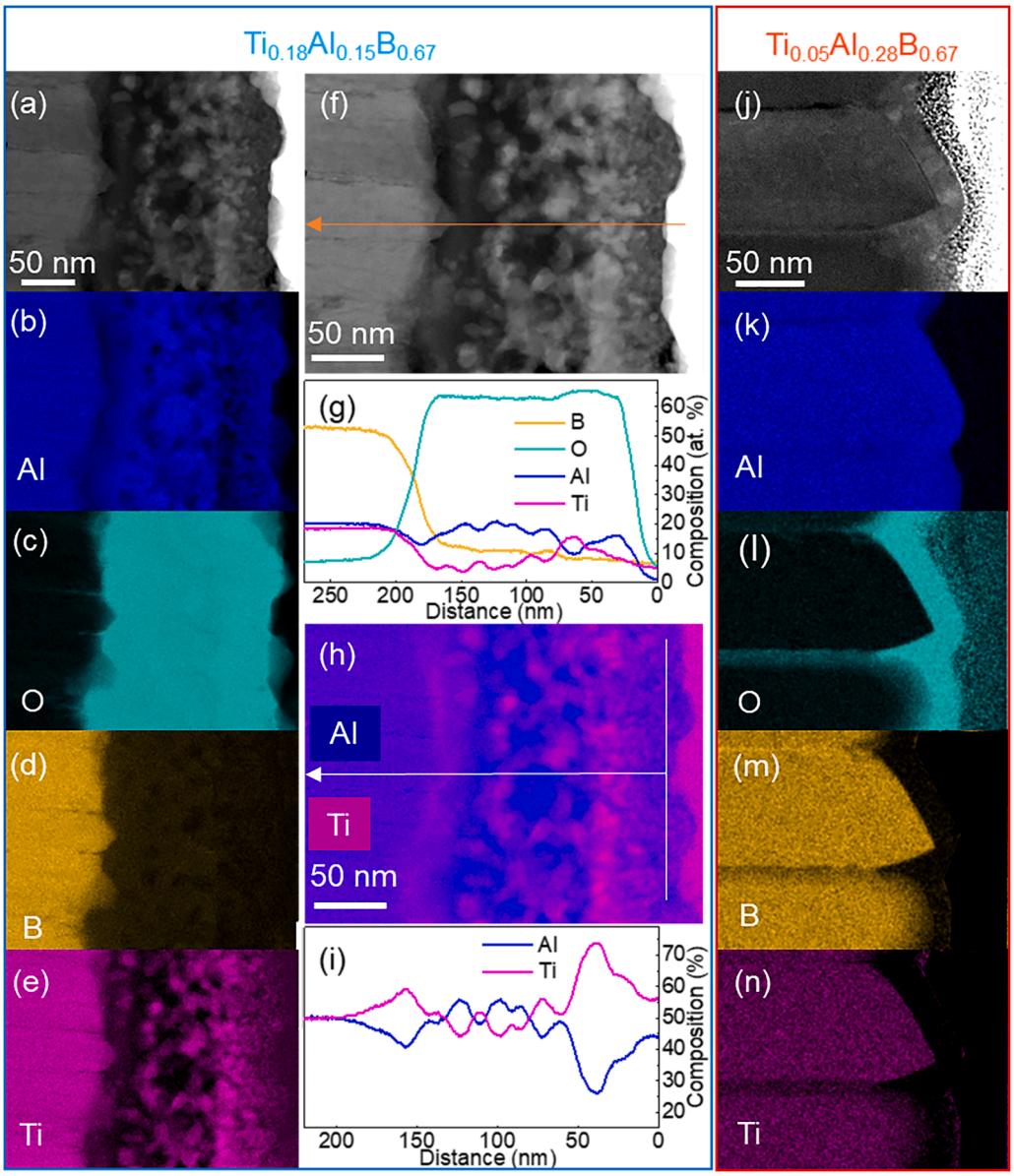


Fig. 8. STEM HAADF image and EDX line scans and elemental mapping for $Ti_{0.18}Al_{0.15}B_{0.67}$ from (a) to (i) and for $Ti_{0.05}Al_{0.28}B_{0.67}$ from (j) to (n) at 700 °C for 4 h.

$>$ 15 and $<$ 21 at.% is subject to future investigations, from the data communicated above, it is evident that a necessary requirement for the formation of a passivating oxide scale is a critical Al concentration. Only if sufficient Al is present in $Ti_{0.33-x}Al_xB_{0.67}$ a dense, passivating, single layer amorphous scale is forming, which is composed of Al and O. As the Al concentration drops below a critical level, the formation of a multi-phase, non-conformal scale exhibiting Al-rich and Ti-rich regions is observed. This scale is clearly porous, B containing and non-passivating in character.

5. Conclusions

The influence of Al concentration variations on the mechanical properties and oxidation behavior of stoichiometric $Ti_{0.33-x}Al_xB_{0.67}$, with x = 0.04, 0.15, 0.21, and 0.28 grown by magnetron sputtering, was investigated by XRD for structural analysis, ERDA for compositional characterization, and STEM imaging for microstructural and morphological studies. By increasing the Al concentration from 4 to 28 at.%, the unit cell volume decreased by 0.8 % which is consistent with *ab initio* calculations with a deviation of $\leq$ 0.9 % compared to the measured values. It was shown that the mechanical properties of diborides are strongly affected by the Al concentration. By addition of Al, the elastic modulus decreases by ~ 7 GPa for each at.% of Al, from 496 ± 19 GPa for $Ti_{0.29}Al_{0.04}B_{0.67}$ to 332 ± 15 GPa for $Ti_{0.05}Al_{0.28}B_{0.67}$ which are with a maximum deviation of $\leq$ 12 % in good agreement with *ab initio* predictions.

The as-deposited diboride coatings were oxidized at 700, 800, and 900 °C for durations of 1, 4, and 8 h, and a bimodal oxidation behavior was observed: While $Ti_{0.33-x}Al_xB_{0.67}$ coatings with 4 and 15 at.% of Al were fully oxidized after exposure to air at 700 °C for 4 h and at 800 °C for 4 h, respectively, forming porous and crystalline mixed Ti-Al oxide layers, the coatings containing 21 and 28 at.% of Al exhibited dense X-ray amorphous scales consisting mainly of Al and O with thicknesses of 319 ± 20 and 273 ± 17 nm, respectively, after 8 h at 900 °C. Nitrides coatings, $Ti_{0.27}Al_{0.21}N_{0.52}$ and $Ti_{0.18}Al_{0.31}N_{0.51}$ with 21 and 31 at.% of Al showed a factor of 8.0 and 1.9 larger oxide scale thicknesses compared to the corresponding diboride coatings containing with 21 and 28 at.% of Al, respectively after 1 h at 900 °C. It was demonstrated that Al addition improved the oxidation resistance where diboride coatings with $\leq$ 15 at.% of Al exhibit non-passive scales while coatings

containing ≥ 21 at.% of Al form passive scales in the here investigated time and temperature ranges. However, this Al addition causes a 32.6 % decrease in elastic modulus (compared to TiB_2) which can be rationalized based on the Al addition induced 22 % reduction in cohesive energy resulting in concomitant bond weakening.

Declaration of competing interest

The authors declare that they have no known competing financial interests or personal relationships that could have appeared to influence the work reported in this paper.

Acknowledgments

This research was funded by the German Research Foundation (DFG SCHN735/42-1). Accelerator operation was supported by the Swedish Research Council VR-RFI (contracts no. 2019-00191 and no. 2017-00646_9) and the Swedish Foundation for Strategic Research (contract RIF14-0053). The authors gratefully acknowledge the computing time granted by the Jülich-Aachen Research Alliance (JARA) HPC section at the IT Center of RWTH Aachen University under the project JARA0151.

Supplementary materials

Supplementary materials associated with this article can be found, in the online version, at doi:10.1016/j.actamat.2024.119829.

References

[1] P.H. Mayrhofer, Thermal Stability and Self-Arrangement of Nanocrystalline Hard Coatings, Springer Netherlands, Dordrecht, 2004, pp. 57–68, https://doi.org/10.1007/1-4020-2222-0_6.
[2] P.H. Mayrhofer, C. Mitterer, J.G. Wen, J.E. Greene, I. Petrov, Self-organized nanocolumnar structure in superhard TiB_2 thin films, Appl. Phys. Lett. 86 (2005) 131909, https://doi.org/10.1063/1.1887824.
[3] W.G. Fahrenholtz, G.E. Hilmas, Ultra-high temperature ceramics: materials for extreme environments, Scr. Mater. 129 (2017) 94–99, https://doi.org/10.1016/j.scriptamat.2016.10.018.
[4] R.G. Munro, Material properties of titanium diboride, J. Res. Natl. Inst. Stand. Technol. 105 (2000) 709, https://doi.org/10.6028/jres.105.057.
[5] J. Besson, F. Valin, P. Lointier, M. Boncoeur, Densification of titanium diboride by hot isostatic pressing and production of near-net-shape components, J. Mater. Eng. Perform. 1 (1992) 637–649, https://doi.org/10.1007/BF02649245.
[6] H. Itoh, S. Naka, T. Matsudaira, H. Hamamoto, Preparation of TiB_2 sintered compacts by hot pressing, J. Mater. Sci. 25 (1990) 533–536, https://doi.org/10.1007/BF00714070.
[7] W.G. Fahrenholtz, G.E. Hilmas, I.G. Talmy, J.A. Zaykoski, Refractory diborides of zirconium and hafnium, J. Am. Ceram. Soc. 90 (2007) 1347–1364, https://doi.org/10.1111/j.1551-2916.2007.01583.x.
[8] S. Ramalingam, L. Zheng, Film-substrate interface stresses and their role in the tribological performance of surface coatings, Tribol. Int. 28 (1995) 145–161, https://doi.org/10.1016/0301-679X(95)98963-E.
[9] R.W. Powell, R.P. Tye, M.J. Hickman, The thermal conductivity of nickel, Int. J. Heat Mass Transf. 8 (1965) 679–688, https://doi.org/10.1016/0017-9310(65)90017-7.
[10] M. Magnuson, L. Hultman, H. Högberg, Review of transition-metal diboride thin films, Vacuum 196 (2022) 110567, https://doi.org/10.1016/j.vacuum.2021.110567.
[11] N.D. Milošević, G.S. Vuković, D.Z. Pavičić, K.D. Maglić, Thermal properties of tantalum between 300 and 2300 K, Int. J. Thermophys. 20 (1999) 1129–1136, https://doi.org/10.1023/A:1022659005050.
[12] I.R. Shein, A.L. Ivanovskii, Elastic properties of mono- and polycrystalline hexagonal AlB_2-like diborides of s, p and d metals from first-principles calculations, J. Phys.: Condens. Matter 20 (2008) 415218, https://doi.org/10.1088/0953-8984/20/41/415218.
[13] F.W. Vahldiek, Electrical resistivity, elastic modulus, and debye temperature of titanium diboride, J. Less Common Metals 12 (1967) 202–209, https://doi.org/10.1016/0022-5088(67)90115-4.
[14] T.A. Saleh, Chapter 1 - Introduction to materials: fundamentals and interactions, in: T.A. Saleh (Ed.), Polymer Hybrid Materials and Nanocomposites, William Andrew Publishing, 2021, pp. 1–25, https://doi.org/10.1016/B978-0-12-813294-4.00006-6.
[15] M. Berger, L. Karlsson, M. Larsson, S. Hogmark, Low stress TiB_2 coatings with improved tribological properties, Thin Solid Films 401 (2001) 179–186, https://doi.org/10.1016/S0040-6090(01)01481-X.
[16] M. Berger, S. Hogmark, Tribological properties of selected PVD coatings when slid against ductile materials, Wear 252 (2002) 557–565, https://doi.org/10.1016/S0043-1648(02)00011-X.
[17] A.S. Dranenko, V.A. Lavrenko, V.N. Talash, Corrosion resistance of nanostructured TiB_2 films in 3% NACl solution, Powder Metall. Met. Ceram. 49 (2010) 174–178, https://doi.org/10.1007/s11106-010-9218-4.
[18] I.I. Korobov, G.V. Kalinnikov, A.V. Ivanov, N.N. Dremova, R.A. Andrievski, S. P. Shilkin, Corrosion resistance of nanostructured films of titanium diboride in mineral acid solutions, Prot. Met. Phys. Chem. Surf. 52 (2016) 618–621, https://doi.org/10.1134/S2070205116040171.
[19] J. Shappirio, J. Finnegan, R. Lux, D. Fox, J. Kwiatkowski, H.P. Kattelus, M. A. Nicolet, TiB_2 and ZrB_2 diffusion barriers in GaAs Ohmic contact technology, J. Vac. Sci. Technol. 3 (1985) 2255–2258, https://doi.org/10.1116/1.572902.
[20] G. Sade, J. Pelleg, Co-sputtered TiB_2 as a diffusion barrier for advanced microelectronics with Cu metallization, Appl. Surf. Sci. 91 (1995) 263–268, https://doi.org/10.1016/0169-4332(95)00129-8.
[21] J.S. Chen, J.L. Wang, Diffusion barrier properties of sputtered TiB_2 between Cu and Si, J. Electrochem. Soc. 147 (2000) 1940, https://doi.org/10.1149/1.1393462.
[22] J.L. Wang, J.S. Chen, TiB_2 as a diffusion barrier for Cu/<Si>metallization, MRS Online Proc. Library 563 (1999) 33–38, https://doi.org/10.1557/PROC-563-33.
[23] F. Kunc, J. Musil, P.H. Mayrhofer, C. Mitterer, Low-stress superhard TiB_2 films prepared by magnetron sputtering, Surf. Coat. Technol. 174-175 (2003) 744–753, https://doi.org/10.1016/S0257-8972(03)00425-0.
[24] S.K. Mishra, P.K.P. Rupa, L.C. Pathak, Surface and nanoindentation studies on nanocrystalline titanium diboride thin film deposited by magnetron sputtering, Thin Solid Films 515 (2007) 6884–6889, https://doi.org/10.1016/j.tsf.2007.02.076.
[25] C.M.T. Sanchez, B.R. Plata, M.E.H.M. da Costa, F.L. Freire, Titanium diboride thin films produced by dc-magnetron sputtering: structural and mechanical properties, Surf. Coat. Technol. 205 (2011) 3698–3702, https://doi.org/10.1016/j.surfcoat.2011.01.014.
[26] N. Panich, Y. Sun, Effect of substrate rotation on structure, hardness and adhesion of magnetron sputtered TiB_2 coating on high speed steel, Thin Solid Films 500 (2006) 190–196, https://doi.org/10.1016/j.tsf.2005.11.055.
[27] W. Dai, T. Zhang, J. Yang, R. Sun, J. Xu, Morphological analysis of TiB_2 thin film prepared by rf magnetron sputtering, J. Vac. Sci. Technol. 26 (2008) 610–615, https://doi.org/10.1116/1.2943642.
[28] N. Nedfors, A. Mockute, J. Palisaitis, P.O.Å. Persson, L.-Å. Näslund, J. Rosen, Influence of pulse frequency and bias on microstructure and mechanical properties of TiB_2 coatings deposited by high power impulse magnetron sputtering, Surf. Coat. Technol. 304 (2016) 203–210, https://doi.org/10.1016/j.surfcoat.2016.06.086.
[29] N. Nedfors, O. Vozniy, J. Rosen, Effect of synchronized bias in the deposition of TiB2 thin films using high power impulse magnetron sputtering, J. Vac. Sci. Technol. 36 (2018), https://doi.org/10.1116/1.5003194.
[30] B. Bakhit, I. Petrov, J.E. Greene, L. Hultman, J. Rosén, G. Greczynski, Controlling the B/Ti ratio of TiBx thin films grown by high-power impulse magnetron sputtering, J. Vac. Sci. Technol. 36 (2018) 030604, https://doi.org/10.1116/1.5026445.
[31] M.N. Polyakov, M. Morstein, X. Maeder, T. Nelis, D. Lundin, J. Wehrs, J.P. Best, T. E.J. Edwards, M. Döbeli, J. Michler, Microstructure-driven strengthening of TiB_2 coatings deposited by pulsed magnetron sputtering, Surf. Coat. Technol. 368 (2019) 88–96, https://doi.org/10.1016/j.surfcoat.2019.04.042.
[32] J. Thörnberg, J. Palisaitis, N. Hellgren, F.F. Klimashin, N. Ghafoor, I. Zhirkov, C. Azina, J.-L. Battaglia, A. Kusiak, M.A. Sortica, J.E. Greene, L. Hultman, I. Petrov, P.O.Å. Persson, J. Rosen, Microstructure and materials properties of understoichiometric TiB_x thin films grown by HiPIMS, Surf. Coat. Technol. 404 (2020) 126537, https://doi.org/10.1016/j.surfcoat.2020.126537.
[33] N. Kalfagiannis, G. Volonakis, L. Tsetseris, S. Logothetidis, Excess of boron in TiB_2 superhard thin films: a combined experimental andab initiostudy, J. Phys. D: Appl. Phys. 44 (2011) 385402, https://doi.org/10.1088/0022-3727/44/38/385402.
[34] J. Thörnberg, B. Bakhit, J. Palisaitis, N. Hellgren, L. Hultman, G. Greczynski, P.O. Å. Persson, I. Petrov, J. Rosen, Improved oxidation properties from a reduced B content in sputter-deposited TiB_x thin films, Surf. Coat. Technol. 420 (2021) 127353, https://doi.org/10.1016/j.surfcoat.2021.127353.
[35] J. Neidhardt, S. Mráz, J.M. Schneider, E. Strub, W. Bohne, B. Liedke, W. Möller, C. Mitterer, Experiment and simulation of the compositional evolution of Ti–B thin films deposited by sputtering of a compound target, J. Appl. Phys. 104 (2008) 063304, https://doi.org/10.1063/1.2978211.
[36] N. Hellgren, J. Thörnberg, I. Zhirkov, M.A. Sortica, I. Petrov, J.E. Greene, L. Hultman, J. Rosen, High-power impulse magnetron sputter deposition of TiB_x thin films: effects of pressure and growth temperature, Vacuum 169 (2019) 108884, https://doi.org/10.1016/j.vacuum.2019.108884.
[37] D.R. Lide, CRC Handbook of Chemistry and Physics, CRC Press, 2004.
[38] S. Mollica, D. Sood, P. Evans, J. Noorman, N. Dytlewski, N. Brack, P. Pigram, K. Latham, Effect of aluminium ion implantation on the oxidation resistance of DC magnetron sputter-deposited TiB_2 thin films, Surf. Coat. Technol. 177 (2004) 185–197, https://doi.org/10.1016/j.surfcoat.2003.06.027.
[39] A. Tampieri, A. Bellosi, Oxidation of monolithic TiB_2 and of Al_2O_3-TiB_2 composite, J. Mater. Sci. 28 (1993) 649–653, https://doi.org/10.1007/BF01151240.
[40] V.B. Voitovich, V.A. Lavrenko, V.M. Adejev, High-temperature oxidation of titanium diboride of different purity, Oxid. Metals 42 (1994) 145–161, https://doi.org/10.1007/BF01061928.
[41] M. Barandika, J. Echeberria, J. Sanchez, F. Castro, Oxidation resistance and microstructure of the oxide layers for TiB2-based cermets, J. Mater. Chem. 8 (1998) 1851–1857, https://doi.org/10.1039/A801121D.

[42] S. Dorri, J. Palisaitis, G. Greczynski, I. Petrov, J. Birch, L. Hultman, B. Bakhit, Oxidation kinetics of overstoichiometric TiB_2 thin films grown by DC magnetron sputtering, Corros. Sci. 206 (2022) 110493, https://doi.org/10.1016/j.corsci.2022.110493.
[43] Y.H. Koh, S.Y. Lee, H.E. Kim, Oxidation behavior of titanium boride at elevated temperatures, J. Am. Ceram. Soc. 84 (2001) 239–241, https://doi.org/10.1111/j.1151-2916.2001.tb00641.x.
[44] X. Cai, S. Ding, K. Wen, L. Xu, H. Xue, S. Xin, T. Shen, Unmasking the anomalous rapid oxidation of refractory TiB_2 at low temperatures, J. Eur. Ceram. Soc. 41 (2021) 5100–5108, https://doi.org/10.1016/j.jeurceramsoc.2021.04.011.
[45] B. Bakhit, J. Palisaitis, J. Thörnberg, J. Rosen, P.O.Å. Persson, L. Hultman, I. Petrov, J.E. Greene, G. Greczynski, Improving the high-temperature oxidation resistance of TiB_2 thin films by alloying with Al, Acta Mater. 196 (2020) 677–689, https://doi.org/10.1016/j.actamat.2020.07.025.
[46] R. Naraparaju, K. Maniya, A. Murchie, W.G. Fahrenholtz, G.E. Hilmas, Effect of moisture on the oxidation behavior of ZrB_2, J. Am. Ceram. Soc. 104 (2021) 1058–1066, https://doi.org/10.1111/jace.17500.
[47] J. Thörnberg, S. Mráz, J. Palisaitis, F.F. Klimashin, P. Ondracka, B. Bakhit, P. Polcik, S. Kolozsvari, L. Hultman, I. Petrov, P.O.Å. Persson, J.M. Schneider, J. Rosen, Oxidation resistance and mechanical properties of sputter-deposited $Ti_{0.9}Al_{0.1}B_{2-y}$ thin films, Surf. Coat. Technol. 442 (2022) 128187, https://doi.org/10.1016/j.surfcoat.2022.128187.
[48] A.H. Navidi Kashani, S. Mráz, D.M. Holzapfel, M. Hans, L. Löfler, P. Ondračka, D. Primetzhofer, J.M. Schneider, Synthesis and oxidation behavior of $Ti_{0.35}Al_{0.65}B_y$ (y=1.7–2.4) coatings, Surf. Coat. Technol. 442 (2022) 128190, https://doi.org/10.1016/j.surfcoat.2022.128190.
[49] A. Mockute, J. Palisaitis, N. Nedfors, P. Berastegui, E. Broitman, B. Alling, L. Å. Näslund, L. Hultman, J. Patscheider, U. Jansson, P.O.Å. Persson, J. Rosen, Synthesis and characterization of $(Ti_{1-x}Al_x)B_{2+\Delta}$ thin films from combinatorial magnetron sputtering, Thin Solid Films 669 (2019) 181–187, https://doi.org/10.1016/j.tsf.2018.10.042.
[50] M. Stüber, H. Riedl, T. Wojcik, S. Ulrich, H. Leiste, P.H. Mayrhofer, Microstructure of Al-containing magnetron sputtered TiB2 thin films, Thin Solid Films 688 (2019) 137361, https://doi.org/10.1016/j.tsf.2019.06.011.
[51] N. Nedfors, S. Mráz, J. Palisaitis, P.O.Å. Persson, H. Lind, S. Kolozsvari, J. M. Schneider, J. Rosen, Influence of the Al concentration in Ti-Al-B coatings on microstructure and mechanical properties using combinatorial sputtering from a segmented TiB_2/AlB_2 target, Surf. Coat. Technol. 364 (2019) 89–98, https://doi.org/10.1016/j.surfcoat.2019.02.060.
[52] G. Greczynski, S. Mráz, L. Hultman, J.M. Schneider, Venting temperature determines surface chemistry of magnetron sputtered TiN films, Appl. Phys. Lett. 108 (2016) 041603, https://doi.org/10.1063/1.4940974.
[53] P. Ström, D. Primetzhofer, Ion beam tools for nondestructive in-situ and in-operando composition analysis and modification of materials at the Tandem Laboratory in Uppsala, J. Instrument. 17 (2022) P04011, https://doi.org/10.1088/1748-0221/17/04/P04011.
[54] Y. Zhang, H.J. Whitlow, T. Winzell, I.F. Bubb, T. Sajavaara, K. Arstila, J. Keinonen, Detection efficiency of time-of-flight energy elastic recoil detection analysis systems, Nucl. Instrum. Methods Phys. Res. Sec. B 149 (1999) 477–489, https://doi.org/10.1016/S0168-583X(98)00963-X.
[55] P. Ström, P. Petersson, M. Rubel, G. Possnert, A combined segmented anode gas ionization chamber and time-of-flight detector for heavy ion elastic recoil detection analysis, Rev. Sci. Instrum 87 (2016) 103303, https://doi.org/10.1063/1.4963709.
[56] W.C. Oliver, G.M. Pharr, An improved technique for determining hardness and elastic modulus using load and displacement sensing indentation experiments, J. Mater. Res. 7 (1992) 1564–1583, https://doi.org/10.1557/JMR.1992.1564.
[57] P. Hohenberg, W. Kohn, Inhomogeneous Electron Gas, Phys. Rev. 136 (1964) B864–B871, https://doi.org/10.1103/PhysRev.136.B864.
[58] W. Kohn, L.J. Sham, Self-Consistent Equations Including Exchange and Correlation Effects, Phys. Rev. 140 (1965) A1133–A1138, https://doi.org/10.1103/PhysRev.140.A1133.
[59] G. Kresse, J. Hafner, Ab initio molecular dynamics for liquid metals, Phys. Rev. B 47 (1993) 558–561, https://doi.org/10.1103/PhysRevB.47.558.
[60] G. Kresse, J. Furthmüller, Efficiency of ab-initio total energy calculations for metals and semiconductors using a plane-wave basis set, Comput. Mater. Sci. 6 (1996) 15–50, https://doi.org/10.1016/0927-0256(96)00008-0.
[61] J.P. Perdew, K. Burke, M. Ernzerhof, Generalized Gradient Approximation Made Simple, Phys. Rev. Lett. 77 (1996) 3865–3868, https://doi.org/10.1103/PhysRevLett.77.3865.
[62] M. Dahlqvist, J. Rosen, Impact of vacancies on structure, stability and properties of hexagonal transition metal diborides, MB2 (M=Sc, Y, Ti, Zr, Hf, V, Nb, Ta, Cr, Mo, W, Mn, and Fe), Materialia 26 (2022) 101629, https://doi.org/10.1016/j.mtla.2022.101629.
[63] A. van de Walle, P. Tiwary, M. de Jong, D.L. Olmsted, M. Asta, A. Dick, D. Shin, Y. Wang, L.Q. Chen, Z.K. Liu, Efficient stochastic generation of special quasirandom structures, Calphad 42 (2013) 13–18, https://doi.org/10.1016/j.calphad.2013.06.006.
[64] R. Yu, J. Zhu, H.Q. Ye, Calculations of single-crystal elastic constants made simple, Comput. Phys. Commun. 181 (2010) 671–675, https://doi.org/10.1016/j.cpc.2009.11.017.
[65] R. Hill, The elastic behaviour of a crystalline aggregate, Proc. Phys. Soc. Sec A 65 (1952) 349–354, https://doi.org/10.1088/0370-1298/65/5/307.
[66] J.M. Schneider, K. Larsson, J. Lu, E. Olsson, B. Hjörvarsson, Role of hydrogen for the elastic properties of alumina thin films, Appl. Phys. Lett. 80 (2002) 1144–1146, https://doi.org/10.1063/1.1448389.
[67] J.A. Dean, Lange's handbook of chemistry, Citeseer (1999).
[68] J. Paier, M. Marsman, K. Hummer, G. Kresse, I.C. Gerber, J.G. Ángyán, Screened hybrid density functionals applied to solids, J. Chem. Phys. 124 (2006) 154709, https://doi.org/10.1063/1.2187006.
[69] O. Eriksson, et al., Electronic structure calculations of phase stability: cohesive and elastic properties, in: K.H.J. Buschow, R.W. Cahn, M.C. Flemings, B. Ilschner, E. J. Kramer, S. Mahajan, et al. (Eds.), Encyclopedia of Materials: Science and Technology, Elsevier, Oxford, 2003, pp. 1–11, https://doi.org/10.1016/B0-08-043152-6/01872-6.
[70] M. Hans, L. Patterer, D. Music, D.M. Holzapfel, S. Evertz, V. Schnabel, B. Stelzer, D. Primetzhofer, B. Völker, B. Widrig, A.O. Eriksson, J. Ramm, M. Arndt, H. Rudigier, J.M. Schneider, Stress-dependent elasticity of TiAlN coatings, Coatings 9 (2019) 24, https://doi.org/10.3390/coatings9010024.
[71] S. Karimi Aghda, D. Music, Y. Unutulmazsoy, H.H. Sua, S. Mráz, M. Hans, D. Primetzhofer, A. Anders, J.M. Schneider, Unravelling the ion-energy-dependent structure evolution and its implications for the elastic properties of (V,Al)N thin films, Acta Mater. 214 (2021) 117003, https://doi.org/10.1016/j.actamat.2021.117003.
[72] B. Bakhit, D. Primetzhofer, E. Pitthan, M.A. Sortica, E. Ntemou, J. Rosen, L. Hultman, I. Petrov, G. Greczynski, Systematic compositional analysis of sputter-deposited boron-containing thin films, J. Vac. Sci. Technol. 39 (2021) 063408, https://doi.org/10.1116/6.0001234.
[73] S. Karimi Aghda, D.M. Holzapfel, D. Music, Y. Unutulmazsoy, S. Mráz, D. Bogdanovski, G. Fidanboy, M. Hans, D. Primetzhofer, A.S.J. Méndez, A. Anders, J.M. Schneider, Ion kinetic energy- and ion flux-dependent mechanical properties and thermal stability of (Ti,Al)N thin films, Acta Mater. 250 (2023) 118864, https://doi.org/10.1016/j.actamat.2023.118864.
[74] C. Fuger, R. Hahn, A. Hirle, P. Kutrowatz, M. Weiss, A. Limbeck, O. Hunold, P. Polcik, H. Riedl, Revisiting the origins of super-hardness in TiB2+z thin films – Impact of growth conditions and anisotropy, Surf. Coat. Technol. 446 (2022) 128806, https://doi.org/10.1016/j.surfcoat.2022.128806.
[75] M. Bartosik, C. Rumeau, R. Hahn, Z.L. Zhang, P.H. Mayrhofer, Fracture toughness and structural evolution in the TiAlN system upon annealing, Sci. Rep. 7 (2017) 16476, https://doi.org/10.1038/s41598-017-16751-1.
[76] A. Bahr, O. Beck, T. Glechner, A. Grimmer, T. Wojcik, P. Kutrowatz, J. Ramm, O. Hunold, S. Kolozsvári, P. Polcik, E. Ntemou, D. Primetzhofer, H. Riedl, Quaternary diborides—Improving the oxidation resistance of $TiB_{2\pm z}$ coatings by disilicide alloying, Mater. Res. Lett. 11 (2023) 733–741, https://doi.org/10.1080/21663831.2023.2225554.
[77] C. Notthoff, M. Winterer, A. Beckel, M. Geller, J. Heindl, Spatial high resolution energy dispersive X-ray spectroscopy on thin lamellas, Ultramicroscopy 129 (2013) 30–35, https://doi.org/10.1016/j.ultramic.2013.02.008.